

Strong-field ionization and high-order-harmonic generation during polyatomic molecular dynamics of N_2O_4

Michael Spanner,¹ Jochen Mikosch,¹ Andrey E. Boguslavskiy,¹ Margaret M. Murnane,² Albert Stolow,¹ and Serguei Patchkovskii¹

¹*Steacie Institute for Molecular Sciences, National Research Council of Canada, Ottawa, Ontario, Canada K1A 0R6*

²*JILA and Department of Physics, University of Colorado and National Institute of Standards and Technology, Boulder, Colorado 80309-0440, USA*

(Received 2 September 2011; published 29 March 2012)

We present state-of-the-art *ab initio*-type computations of strong-field ionization (SFI) and the single-molecule response contribution to high-order-harmonic generation (HHG) in the polyatomic molecule N_2O_4 . The numerical method uses a mixed orbital- and grid-based approach to model the multielectron bound states and single-electron continuum. The effects of ionic-core attraction and Coulomb-mediated interchannel coupling are rigorously included. We show that full-dimensionality time-dependent multielectron computations of SFI and HHG in polyatomic molecules are now feasible. The computational results indicate that (a) SFI yields in N_2O_4 are dominated by a single ionic state (the A_g state), and are strongly modulated by the N-N stretch coordinate; and (b) the HHG radiating dipole as a function of the N_2O_4 N-N stretch is dominated by the same, single state. The molecular-beam coincidence measurements presented here support the computational results. Due to the differences in the estimated vibrational amplitude, however, the computations are not in full agreement with previous HHG data.

DOI: [10.1103/PhysRevA.85.033426](https://doi.org/10.1103/PhysRevA.85.033426)

PACS number(s): 33.20.Xx, 33.80.Rv, 42.65.Ky

I. INTRODUCTION

Attosecond science [1], driven by the underlying processes of strong-field ionization (SFI) and high-order-harmonic generation (HHG) [2], offers the promise of measuring electronic motion with angstrom and subfemtosecond resolution. In the process of HHG, an atom or molecule is first ionized by a strong laser field. The liberated electron is then accelerated in the laser field to tens of eV and recombines with the parent ion, emitting its energy as a burst of XUV radiation. Although much work in this field has focused on the atomic and small-molecule limits where existing semianalytical strong-field-ionization theories remain applicable, experiments on polyatomic systems have begun to appear [3–7]. The electronic and structural properties of these polyatomic systems lie far from the expected range of validity of the simple theories. Even more challenging to theory is the use of HHG in time-resolved probing of polyatomic molecular dynamics [4]. In such situations, both vibrational and electronic structures generally evolve as a function of time [8]. In order to model the results of such measurements, we will require theories of SFI and HHG which extend to real polyatomic systems.

Here, we apply a recently developed *ab initio*-type method [9], potentially capable of handling SFI and HHG in gas phase molecules of arbitrary size. We use the previously studied N_2O_4 system [4] as the target for the theoretical method. In past work [4], a vibrational wave packet on the electronic-ground-state surface of neutral N_2O_4 was prepared via impulsive stimulated Raman scattering. The wave packet exhibited large-amplitude motion along the symmetric N-N stretch coordinate. The wave-packet dynamics were probed using a time-delayed intense probe pulse which generated the HHG signal, with all observed harmonic orders maximizing at the outer turning point. Using traditional tunneling theories for the SFI and HHG processes, the time-resolved HHG spectra were interpreted in

terms of switching between two active ionic continua, with the B_{2g} state dominating at the inner turning point and the A_g ground state dominating at the outer turning point.

The method employed here [9] uses a full-dimensionality multielectron time-dependent mixed orbital- and grid-based approach to model the multielectron bound states and the single-electron continuum. The effects of ionic-core attraction and Coulomb-mediated interchannel coupling are rigorously included. To mimic a full nuclear wave-packet dynamics calculation, we apply this approach to model single-molecule response in HHG and SFI in N_2O_4 as a function of the N-N bond length. The A_g -state ionization dynamics dominates over the whole range of internuclear distances considered. The B_{2g} excited state does play a minor role, but mostly beyond the outer turning point where it affects the total HHG signal through destructive interference with the dominant A_g channel. The results show a strong bond-length dependence of the angle-resolved ionization yields for the B_{2g} excited-state channel but little bond-length dependence for the A_g ground-state channel. We note that, while our calculations do predict modulations of the HHG yield as a function of the vibrational coordinate, they do not fully reproduce the modulations seen in the HHG data of Ref. [4]. However, they do clearly demonstrate that a two-state tunneling-type calculation, as given in Ref. [4], is insufficient. Specifically, for the comparison of the A_g and B_{2g} ionization rates, the authors of Ref. [4] used the Keldysh rate $a_K = \exp[-(2/3)(2I_p)^{3/2}/E_0]$ which incorporates only the ionization potential I_p and the peak field strength E_0 , but not the details of the electronic structure or the ion potential. The present *ab-initio*-type calculations are a significant improvement over the approximate methods used in Ref. [4] and suggest a necessary departure from traditional tunneling theories developed for atomiclike systems, as high-order-harmonic probing and attosecond methods extend into the regime of polyatomic molecules. As applications of *ab*

initio-type methods are expanded to include even more electronic continua, laser-driven interchannel coupling, coherent vibrational wave-packet effects, focal volume averaging, and propagation effects, we anticipate the ability to compare directly with time-resolved HHG studies of dynamics in polyatomic molecules.

II. SFI SIMULATIONS

We focus primarily on the independent-ionic-channel version of the method [9]. That is, we consider ionization to multiple final ionic states (the A_g and B_{2g} states) but calculate ionization to each state individually, neglecting ionic interchannel couplings. The independent-channel version of Ref. [9] can be used as the starting point from which all formulas used in the theoretical analysis of Ref. [4] can be derived by making further approximations. In particular, the present method allows for the rigorous inclusion of the ionic electrostatic binding potential during ionization, recollision, and recombination, all of which were either neglected or included only semiclassically in the previous model [4]. In order to facilitate the comparison, the present model uses the same quantum chemistry calculations used in Ref. [4] to obtain the required potential energy surfaces, ionic potentials, and Dyson orbitals. We have also performed coupled-channel calculations that include coupling terms between the ionic states, arising from the Coulomb interaction between the continuum electron and the ionic cores. Since laser-driven coupling [also known as nonadiabatic multielectron (NME) dynamics [10]] between the A_g and B_{2g} ionic states is forbidden by symmetry due to the vanishing transition dipole, the Coulomb interaction is the only coupling mechanism present. For these states we find negligible qualitative differences between the coupled and uncoupled results, further justifying the use of the uncoupled-channel calculations. Other states not included here could potentially be coupled.

We use a laser pulse at $\lambda = 800$ nm, with a sine² envelope, full width at half maximum of 4.8 fs, and 1.5×10^{14} W/cm² peak intensity. The calculations employ three-dimensional Cartesian grids extending to ± 25 a.u. in all directions. Absorbing boundaries [11] with width of 4.3 a.u. are used at the grid edges. For this grid size and intensity, the long trajectories are mostly absorbed at the grid edges before they recollide, and therefore the calculated HHG spectra effectively included the short trajectories alone. Ionization and single-molecule HHG yields are calculated for different angles between the molecular frame and the polarization direction of the laser pulse using Lebedev angular grids of the ninth order [12]. Total yields are obtained by integrating over all angles.

We first consider the ionic-state-resolved ionization yields at selected N-N internuclear distances, shown in Fig. 1. In contrast to the previous model [4], where the ionization yield to the B_{2g} state dominated at small bond lengths, the present results predict that ionization to the A_g dominates at all bond lengths. Even for the shortest bond length (1.4 Å), the yield to the A_g state is six times larger than the B_{2g} state, despite B_{2g} possessing a lower ionization potential at this geometry. The qualitative explanation for the suppression of the B_{2g} state lies with the orbital symmetries. The Dyson orbitals, shown in Fig. 2, represent the initial single-particle state of the ionizing

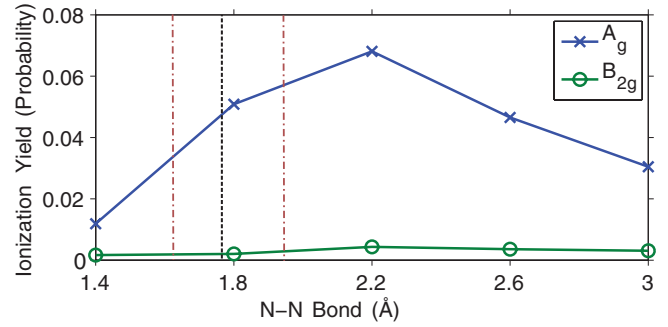


FIG. 1. (Color online) Calculated probability of forming the A_g and B_{2g} cation states via SFI as a function of the N-N bond length. See the text for the parameters of the laser pulse used in the simulation. The vertical dashed line indicates the neutral equilibrium N-N bond length (1.76 Å). The vertical dash-dotted lines give the estimated amplitude of vibrational motion in our SFI experiment ($-0.14/\pm 0.18$ Å; for details see the text).

electron [9]. In the Koopmans approximation they become the highest occupied molecular orbital (HOMO) and the next lower orbital (HOMO-1). For diatomics, it has been shown [13] that orbitals with nodes along dominant axes of symmetry have suppressed ionization rates. Strong-field ionization picks out the low-momentum components of the ionizing orbitals on the order of $k \approx 2\sqrt{\omega}$ [13]. Orbitals with nodes along the dominant axes of symmetry, such as the B_{2g} state, have suppressed amplitude of the low-momentum components and consequently show a suppression of ionization. In contrast, orbitals without nodes along the dominant axes of symmetry, such as the A_g state, have no expected suppression of the low-momentum components and show no suppression in ionization.

Of further interest to the ionization dynamics are the angle-resolved ionization yields, shown in Fig. 2, where the angle is between the molecular frame and the electric field polarization direction of the laser. The conventional wisdom derived from angle-resolved ionization rates for diatomics and

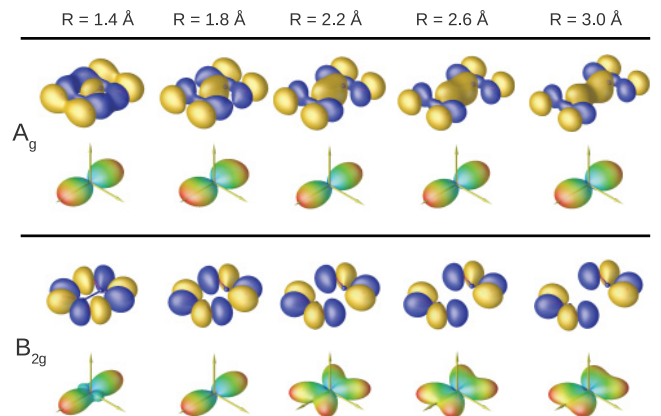


FIG. 2. (Color online) Dyson orbitals (upper rows of each panel) and normalized angle-dependent ionization yields (bottom rows) as a function of the N-N bond length for the two ionic states considered in this work.

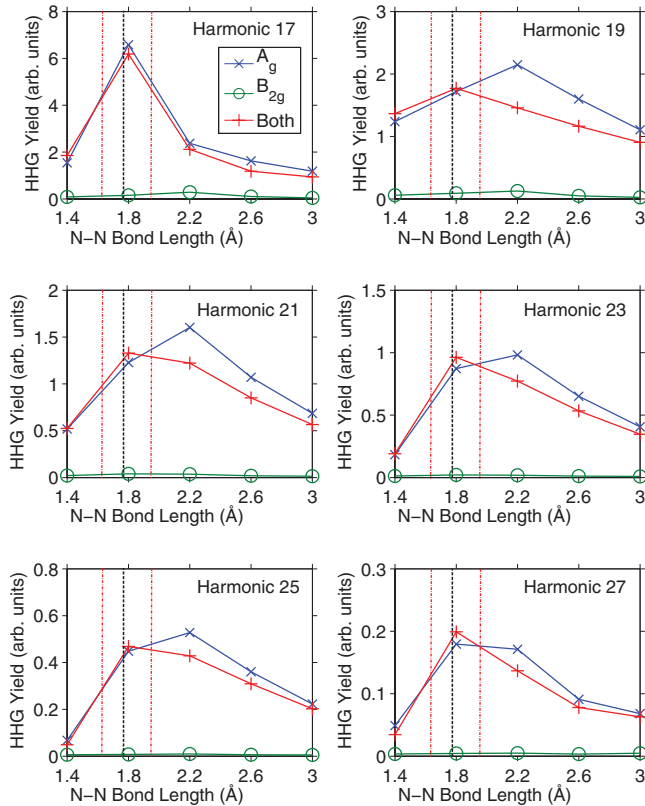


FIG. 3. (Color online) Bond-length-dependent HHG signal: HHG from the A_g channel (\times), HHG from the B_{2g} channel (\circ), and the coherent sum of the two channel contributions ($+$). Also see Fig. 1 caption.

triatomic suggests that angular ionization rates qualitatively follow the nodal structure of the ionizing Dyson orbital [14]. There is typically suppression of the ionization when the electric field is parallel to a nodal plane and enhancement when the electric field is parallel to an extended orbital lobe. The trend is maintained for the A_g state in the present calculations; suppression of ionization is seen when the electric field of the laser is parallel to dominant nodal planes of the Dyson orbital. However, it is strongly violated for the B_{2g} state as the N-N bond is varied. For small bond lengths, this state ionizes preferentially when the electric field is parallel to the N-N bond, despite the fact that there is a nodal plane along this direction. For larger N-N bond lengths, the preferred ionization direction moves away from the N-N bond axis.

III. HHG SIMULATIONS

We now turn to the calculation of HHG signals. The single-molecule HHG yield was calculated using the length form of the dipole operator. The HHG signal as a function of N-N bond length for harmonic orders 17 to 27 is shown in Fig. 3. The figure plots the HHG yield from the two ionic states independently, as well as their coherent sum. These HHG yields include the coherent sum of emission coming from all angles of the molecular axes relative to the electric field polarization direction. We emphasize that the method of Ref. [9] is a realization of the time-dependent Schrödinger equation and does not assume any type of

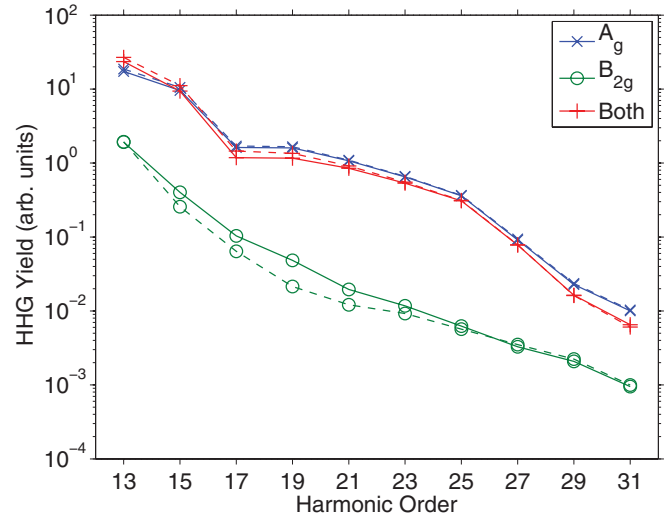


FIG. 4. (Color online) HHG spectra calculated with (dashed curves) and without (solid curves) Coulomb interchannel coupling for a N-N distance of 2.6 Å. Shown are the HHG yields for the A_g channel (\times), the B_{2g} channel (\circ), and the coherent sum of the two channel contributions ($+$).

three-step decomposition of the HHG process. Thus, the ionization yields discussed above and the HHG yields presented in Fig. 3 all come from the same time-dependent calculation, and there is no ambiguity in either assigning an instantaneous ionization rate or assigning the harmonic photon energy to a particular recollision energy. From the calculated HHG intensities, it can be seen that the A_g state dominates over the whole range of N-N bond lengths considered, whereas HHG from the B_{2g} state remains about an order of magnitude lower for all bond lengths. When the HHG signal from both states is added coherently, as is the case in experiment, the B_{2g} state does have an effect on the total HHG yield. It lowers the yield at large N-N bond lengths through destructive interference with the A_g channel. The predictions of Fig. 3, over the 1.6–2.2 Å bond-length range, differ from the experimental results [4], which saw all measured HHG orders peak in phase at the outer turning point. The differences could be due to a number of factors, including ionic states not included here, phase-matching effects, pulse shape, and focal volume averaging, etc.

In Fig. 4, we present coupled-channel simulations of the HHG signal for an N-N bond length of 2.6 Å. These more elaborate calculations include the Coulomb interaction between the continuum electron and the ionic cores. Coulomb coupling of the ionic states can occur during the ionization [15] and recollision [16] steps. As can be seen in Fig. 4, these Coulomb couplings between A_g and B_{2g} cause only small quantitative changes in the HHG yields, thus justifying the use of the uncoupled simulations.

IV. SFI MEASUREMENTS

The computed HHG modulations of Fig. 3 do not yet fully match the experimentally observed time-resolved HHG modulations [4]. This is likely due to the need to include

coherent vibrational wave-packet effects, higher-lying ionic states, laser-driven interchannel coupling to these additional states, and phase-matching and propagation effects. In order to test the present theoretical results under different conditions that allow measurements of isolated molecular ionization, we developed molecular-beam photoelectron-photoion coincidence SFI yield measurements of vibrational wave-packet dynamics of N_2O_4 . Briefly, a vibrational wave packet in the N-N stretch coordinate is prepared by impulsive stimulated Raman scattering (SRS) using an ultrashort laser pulse (35 fs) at $\lambda = 2100$ nm. We measure the SFI yield as a function of time delay with respect to the SRS pump using a probe laser pulse at $\lambda = 800$ nm. In order to minimize focal volume averaging, the 800 nm SFI probe pulse interrogated a small volume within that of the $\lambda = 2100$ nm SRS pump pulse. Furthermore, the molecular beam was tightly skimmed to intersect with only the central third of the Rayleigh range of the laser foci. Spherical reflective focusing optics were implemented so as to minimize chromatic effects. The pump-probe time delay was scanned by a computer-controlled delay stage. The temporal width [full width at half maximum (FWHM)] of the probe pulse was around 35 fs; the multiphoton-ionization cross correlation between pump and probe pulses was around 50 fs. Zero time delay was set by the cross-correlation measurements performed before the scans. Temporal stability was ensured by confirming zero time delay after all scans were complete. The peak intensity of both laser pulses was $I_0 = 0.9 \times 10^{14}$ W/cm², higher than the SRS pump pulse (0.2×10^{14}), but lower than the HHG probe (2×10^{14}) in Ref. [4]. N_2O_4 is supplied at an estimated interaction-region number density of 10^9 cm⁻³ via a stable, continuous supersonic expansion of neat NO_2 . Both the gas reservoir and the nozzle were cooled to -38°C in order to ensure a preexpansion dimer fraction of around 90% at the low target density required for coincidence measurements. Ion and electron yields were collected in coincidence using a large-bore magnetic bottle photoelectron-photoion coincidence (PEPICO) spectrometer.

The pump laser wavelength here is longer than that of Ref. [4] and therefore the amplitude of the wave-packet motion could be different. To estimate the amplitude of the N-N stretching motion, we calculated the polarizability derivative of N_2O_4 with respect to the N-N bond length using numerical differentiation of the unrelaxed static polarizabilities in coupled-cluster theory with single, double, and connected triple excitations [CCSD(T)] using augmented correlation-consistent valence triple-zeta (aug-cc-pVTZ) basis set [17–19]. The N-N bond length was fixed at $R_{\text{N-N}} = 1.786$ and 1.686 Å, with the remaining structural parameters optimized at the CCSD(T)/aug-cc-pVTZ level. The resulting isotropic polarizability derivative $\partial\alpha/\partial r$ is 12.2 bohr². For a 2.1 μm pump wavelength, the differences between the static and frequency-dependent polarizabilities are expected to be negligible. For a pump pulse much shorter than the vibrational period, the overall momentum transfer to the vibrational mode is [20] $p = \frac{1}{4} \frac{\partial\alpha}{\partial r} F_0^2 \int f(t)^2 dt$, where F_0 is the peak amplitude of the electric field, and $f(t)$ is the carrier envelope. [For a Gaussian pulse with FWHM of τ , the envelope integral is $\tau(\pi/\ln 16)^{1/2}$]. The amplitude of the vibration can be estimated from the classical turning points at the energy $p^2/2\mu$, where μ is the reduced mass of the

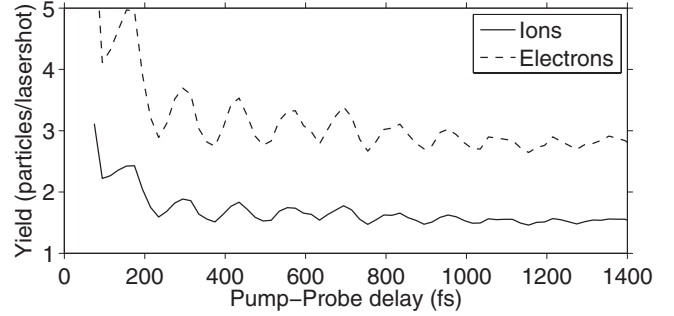


FIG. 5. Coincident photoion and photoelectron yields for wave-packet dynamics in N_2O_4 as a function of pump-probe delay. For details, see the text.

oscillator. For the SRS conditions in our experiment ($I_0 = 0.9 \times 10^{14}$ W/cm²; $\tau = 35$ fs), the resulting vibrational amplitude is $-0.14/+0.18$ Å, based on the anharmonic potential energy curve of Ref. [4].

In Fig. 5 we present the total (i.e., energy- and angle-integrated) photoelectron and photoion yield per laser shot as a function of the pump-probe time delay. The polarizations of pump and probe pulse were parallel. The data were averaged over 9.5×10^4 laser shots at each time delay, accumulated over 19 time-delay scans. Ionization by the SRS pump laser pulse alone resulted in a constant background of around 2.4 electrons and 1.4 ions per laser shot, which was subtracted. (Ion and electron yields differ due to collection and detection efficiencies.) We observed strongly pronounced oscillations in the SFI yield, with the initial modulation depth exceeding 30%. The oscillation period as determined from the data in Fig. 5 (and three similar data sets) is $T = 131.25(0.40)$ fs. The positions of the maxima occur at $\sim nT + T/4$ ($n \in \mathbb{N}^+$), consistent with an initial outward stretch of the N-N bond. For comparison, linear interpolation of the calculated ionization yields (Fig. 1) obtains an $\approx 40\%$ modulation depth, with the yield maximizing for the stretched N-N bond. The oscillation period matches the gas-phase N-N symmetric stretch ν_3 Raman-active mode located at 254 ± 2 cm⁻¹ [21], which corresponds to a period of 131.3 ± 1.0 fs. For these SRS wave-packet dynamics experiments (at $\lambda = 2100$ nm), the SFI yield is modulated in phase with the previously reported HHG modulations [4], both periodically maximizing at $nT + T/4$. These experimental results support the present theoretical model, which suggests that SFI should occur mainly at the outer turning point of the N-N stretch due to the dominance of the A_g ground-state channel.

V. CONCLUSIONS

Our calculations represent one of the most complete simulations of SFI and single-molecule HHG response in a polyatomic molecule to date. It is now feasible to rigorously include in SFI simulations effects of orbital symmetry, structured binding potentials, and Coulomb-driven interchannel couplings. The present example of HHG in N_2O_4 as a function of N-N bond length highlights the importance of effects often neglected in traditional strong-field approximation (SFA)

based approximate methods. The dynamics of polyatomic systems generally involves the motions of the atoms, the rearrangements of the valence electrons, and, importantly, the coupling between these [8]. In such a situation, the simple SFA-based methods are unlikely to apply. As the field of attosecond

science evolves toward dynamics in polyatomic molecules, there is a need for high-level *ab initio* computations of both SFI and HHG. Emerging theoretical methods, such as the one presented here, will play an increasingly important role in this development.

-
- [1] A. Scrinzi *et al.*, *J. Phys. B* **39**, R1 (2006); M. Lein, *ibid.* **40**, R135 (2007).
- [2] P. B. Corkum, *Phys. Rev. Lett.* **71**, 1994 (1993); M. Lewenstein, P. Balcou, M. Y. Ivanov, A. L'Huillier, and P. B. Corkum, *Phys. Rev. A* **49**, 2117 (1994).
- [3] N. L. Wagner *et al.*, *Proc. Natl. Acad. Sci. USA* **103**, 13279 (2006).
- [4] W. Li *et al.*, *Science* **322**, 1207 (2008).
- [5] R. A. Ganeev, L. B. Elouga Bom, J. Abdul-Hadi, M. C. H. Wong, J. P. Brichta, V. R. Bhardwaj, and T. Ozaki, *Phys. Rev. Lett.* **102**, 013903 (2009).
- [6] M. C. H. Wong, J.-P. Brichta, and V. R. Bhardwaj, *Phys. Rev. A* **81**, 061402(R) (2010).
- [7] C. Vozzi *et al.*, *Appl. Phys. Lett.* **97**, 241103 (2010).
- [8] A. Stolow and J. G. Underwood, *Adv. Chem. Phys.* **139**, 497 (2008).
- [9] M. Spanner and S. Patchkovskii, *Phys. Rev. A* **80**, 063411 (2009).
- [10] M. Lezius, V. Blanchet, D. M. Rayner, D. M. Villeneuve, A. Stolow, and M. Y. Ivanov, *Phys. Rev. Lett.* **86**, 51 (2001).
- [11] D. E. Manolopoulos, *J. Chem. Phys.* **117**, 9552 (2002).
- [12] V. I. Lebedev, *USSR Comput. Math. Math. Phys.* **15**, 44 (1975).
- [13] J. Muth-Böhm, A. Becker, and F. H. M. Faisal, *Phys. Rev. Lett.* **85**, 2280 (2000).
- [14] D. Pavičić, K. F. Lee, D. M. Rayner, P. B. Corkum, and D. M. Villeneuve, *Phys. Rev. Lett.* **98**, 243001 (2007); H. Akagi *et al.*, *Science* **325**, 1364 (2009).
- [15] Z. B. Walters and O. Smirnova, *J. Phys. B* **43**, 161002 (2010).
- [16] S. Sukiasyan, C. McDonald, C. Destefani, M. Y. Ivanov, and T. Brabec, *Phys. Rev. Lett.* **102**, 223002 (2009).
- [17] J. F. Stanton, J. Gauss *et al.*, computer code CFOUR (University of Texas at Austin, USA and Universität Mainz, Germany). For the current version, see [<http://www.cfour.de>].
- [18] M. Kállay and J. Gauss, *J. Mol. Struct., Theochem* **768**, 71 (2006).
- [19] R. A. Kendall, T. H. Dunning Jr., and R. J. Harrison, *J. Chem. Phys.* **96**, 6796 (1992).
- [20] Y.-X. Yan, E. B. Gamble Jr., and K. A. Nelson, *J. Chem. Phys.* **83**, 5391 (1985).
- [21] C. Dyer and P. J. Hendra, *Chem. Phys. Lett.* **233**, 461 (1995).